Nano Research 2017, 10(6): 1861–1871
DOI 10.1007/s12274-016-1291-7
Research Article
ISSN 1998-0124
CN 11-5974/O4

A highly sensitive chemical gas detecting transistor based on highly crystalline CVD-grown $MoSe_2$ films

Jongyeol Baek[1,§], Demin Yin[2,§], Na Liu[1,§], Inturu Omkaram[1], Chulseung Jung[1], Healin Im[1], Seongin Hong[1], Seung Min Kim[3], Young Ki Hong[1], Jaehyun Hur[4] (✉), Youngki Yoon[2] (✉), and Sunkook Kim[1] (✉)

[1] *Multi-Functional Nano/Bio Electronics Lab., Kyung Hee University, Gyeonggi 446-701, Republic of Korea*
[2] *Department of Electrical and Computer Engineering & Waterloo Institute for Nanotechnology (WIN), University of Waterloo, Waterloo, ON N2L 3G1, Canada*
[3] *Institute of Advanced Composite Materials, Korea Institute of Science and Technology (KIST), Jeonbuk 565-905, Republic of Korea*
[4] *Department of Chemical and Biological Engineering, Gachon University, Seongnam-si, Gyeonggi 13120, Republic of Korea*
[§] *These authors contributed equally to this work.*

Received: 21 July 2016
Revised: 24 August 2016
Accepted: 14 September 2016

KEYWORDS
transition metal dichalcogenides,
$MoSe_2$,
chemical sensors,
chemical vapor depositon

ABSTRACT

Layered semiconductors with atomic thicknesses are becoming increasingly important as active elements in high-performance electronic devices owing to their high carrier mobilities, large surface-to-volume ratios, and rapid electrical responses to their surrounding environments. Here, we report the first implementation of a highly sensitive chemical-vapor-deposition-grown multilayer $MoSe_2$ field-effect transistor (FET) in a NO_2 gas sensor. This sensor exhibited ultra-high sensitivity (S = ca. 1,907 for NO_2 at 300 ppm), real-time response, and rapid on–off switching. The high sensitivity of our $MoSe_2$ gas sensor is attributed to changes in the gap states near the valence band induced by the NO_2 gas absorbed in the $MoSe_2$, which leads to a significant increase in hole current in the off-state regime. Device modeling and quantum transport simulations revealed that the variation of gap states with NO_2 concentration is the key mechanism in a $MoSe_2$ FET-based NO_2 gas sensor. This comprehensive study, which addresses material growth, device fabrication, characterization, and device simulations, not only indicates the utility of $MoSe_2$ FETs for high-performance chemical sensors, but also establishes a fundamental understanding of how surface chemistry influences carrier transport in layered semiconductor devices.

1 Introduction

In recent years, the sensing of biological and chemical molecules has become increasingly important for environmental, biomedical, and agricultural applications [1–4]. NO_2 is one of the most dangerous environ-

Address correspondence to Jaehyun Hur, hjhhjh76@gmail.com; Youngki Yoon, youngki.yoon@uwaterloo.ca; Sunkook Kim, intel0616@gmail.com

mentally hazardous gas species that we encounter in our daily lives [5]. It has been reported that long-term exposure to NO_2 gas can lead to lung diseases and an increased risk of respiratory symptoms, with the exposure time to NO_2 gas for humans being limited to less than 8 h, even at 3 ppm [6]. In addition, the NO_2 gas generated from automobiles and power plants is thought to contribute to nitric acid rain, which accelerates the degradation of the environment. Consequently, there is an increasing demand for highly sensitive and reliable NO_2 gas sensors to protect human health and to provide timely alarms in the chemical industry.

Field-effect transistors (FETs), which are basic building blocks in electronic circuits, have recently emerged as a novel sensing technology [5, 7–10]. Although there are many resistor-type sensors that can detect various harmful gases [11–13], FET-based gas sensors are generally superior to the simple resistor-type sensors owing to their high sensitivity, large signal-to-noise ratio, short response time, and reliability. The high-sensitivity response of FET sensors is conferred by the gate electrode, which provides extra freedom for current modulation. The sensitivity of FETs can also be evaluated from other parameters, such as subthreshold swing, threshold voltage, and variation of current.

A wide variety of semiconductors have been investigated as active materials for NO_2 sensors, including amorphous organic semiconductors, porous silicon, silicon nanowires, carbon nanotubes, and metal oxide nanowires [5, 14–18]. However, layered semiconductors such as transition metal dichalcogenides (TMDs) have been very rarely investigated for NO_2 sensing, especially in the form of FET-type sensors, despite two-dimensional (2D) materials being promising candidates for chemical sensors owing to their large surface-to-volume ratios [8, 11–13, 19–21].

In the present work, we report the first example of a highly sensitive FET-type NO_2 gas sensor based on a highly crystalline $MoSe_2$ film prepared by chemical vapor deposition (CVD). When the device is exposed to different NO_2 environments, the off-current of the $MoSe_2$ transistor increases exponentially with NO_2 gas concentration, exhibiting a maximum sensitivity (S) of ca. 1,907 at 300 ppm. Device modeling and quantum transport simulations along with the measurement data indicate that the high sensitivity of $MoSe_2$ FETs to NO_2 gas may be attributed to the large variation in the hole current caused by changes in the gap states in the $MoSe_2$, which are, in turn, induced by the absorbed NO_2 gas. Our comparative analysis of FET-based and diode-based sensors demonstrates the considerable advantages of using a gate electrode to boost the sensitivity of devices. Finally, we demonstrate the real-time response and fast switching behavior of a FET-based device, highlighting the robustness and potential of our $MoSe_2$ FET for NO_2 gas sensors.

2 Experimental

2.1 Synthesis of bulk $MoSe_2$

Bulk $MoSe_2$ was grown by a modified CVD method [22]. First, Mo powder (99.95% purity) and Se shot (99.999% purity) were used under low pressure (10^{-5} Torr) to form polycrystalline $MoSe_2$ compounds. Then, the polycrystalline $MoSe_2$ and Mo-coated Si substrate precursors were heated to 1,050 and 1,000 ℃, respectively, to synthesize bulk $MoSe_2$. The $MoSe_2$ grains exhibited hexagonal structures with sizes in the micrometer range.

2.2 Material characterization

The CVD-grown multilayer $MoSe_2$ samples were characterized using atomic force microscopy (AFM), X-ray diffraction (XRD), Raman spectroscopy, and transmission electron microscopy (TEM). The topography of $MoSe_2$ flakes deposited on SiO_2/Si substrates was measured using a PSIA XE7atomic force microscope in non-contact mode. XRD patterns were recorded on a Bruker D8 Advance X-ray diffractometer using Cu Kα radiation. Raman spectra were measured using a high-resolution Raman spectrometer (Invid Raman microscope, Renishaw) with laser excitation at 514.5 nm. The TEM images were obtained using a Tecnai F20 FEI transmission electron microscope at an accelerating voltage of 200 kV.

2.3 Device fabrication and measurements

As-grown $MoSe_2$ was mechanically exfoliated and transferred to an Si/SiO_2 surface. Then, the Si wafer

was immersed in acetone and isopropyl alcohol for 2 h to remove residues. The device was fabricated using conventional photolithography and lift-off methodology. The Ti/Au (20 nm/300 nm) bilayer metal of the source and drain electrodes was deposited using an e-beam evaporator. After patterning, the device was annealed at 200 ℃ for 2 h in an H_2 environment. The electrical properties of the device were measured using a Keithley 4200 semiconductor characterization system.

2.4 Sensor measurement

The fabricated device was wire-bonded to a leadless chip carrier to probe the sample in a vacuum chamber. The schematic of the experimental setup is shown in Fig. S1 (in the Electronic Supplementary Material (ESM)). The sensing experiments were performed by exposing the $MoSe_2$ device to NO_2 diluted with N_2. The NO_2 concentration of the mixed gas was controlled by adjusting the flow rates of the N_2 and NO_2 by means of mass flow controllers. All the gas-sensing experiments and characterizations were performed at room temperature.

2.5 Device modeling and simulations

The transport characteristics were simulated using the non-equilibrium Green's function (NEGF) formalism with an effective mass approximation, self-consistently with Poisson's equation [23]. Since the device shows ambipolar behavior, the electron (n-type) current ($I_{ds,n}$) and hole (p-type) current ($I_{ds,p}$) were calculated separately, and the total current was obtained as $I_{ds} = I_{ds,n} + I_{ds,p}$. Values of $0.55m_0$ and $0.71m_0$ were used for electron and hole effective mass, respectively [24], where m_0 is free electron mass. The following parameters were used for the nominal device: a 15 nm intrinsic monolayer $MoSe_2$ channel ($\varepsilon_r = 6.9$) [25], and a single-gate device structure with a 2.6 nm-thick SiO_2 gate dielectric. Ballistic transport was assumed. These simulation settings can be used to explore the underlying physics, and will not alter our conclusions for larger devices. Schottky barrier (SB) heights for electrons and holes are chosen such that $\Phi_{Bn} + \Phi_{Bp} = E_g$ for multilayer $MoSe_2$ (0.84 eV) [26] in the absence of NO_2 gas. As the NO_2 gas concentration was increased, the effective Φ_{Bp} was varied from 0.74 to 0.34 eV in order to address the extra leakage paths for holes without changing Φ_{Bn} (0.1 eV), and channel doping was also increased (up to 8×10^{18} cm^{-3} for a Φ_{Bp} of 0.34 eV) to take the p-doping effect into account.

3 Results and discussion

Multilayer $MoSe_2$ was prepared by CVD onto a SiO_2 substrate. The details of the synthesis were reported in our previous work [22]. Figures 1(a) and 1(b) show optical microscopy and AFM images of a CVD-grown $MoSe_2$ flake. The thickness of the $MoSe_2$ flake is ca. 41 nm. Since the quality and crystallinity of materials directly affect device performance, we characterized the multilayer $MoSe_2$ using XRD, Raman spectroscopy, and TEM. In the XRD pattern (Fig. 1(c)), prominent peaks appear at 2θ values of 13.72°, 27.65°, 41.96°, and 57.01°, which correspond to the (002), (004), (006), and (008) planes, respectively. This reveals that the $MoSe_2$ has a hexagonal, single-crystalline structure [27]. The strongest peak at 2θ = 13.72°, corresponding to the (002) plane, indicates the preferential growth of the $MoSe_2$ crystallites in this direction. The Raman spectrum of the $MoSe_2$ (Fig. 1(d)) presents several typical peaks. An intense out-of-plane A_{1g} peak appears at 242 cm^{-1}, and weak in-plane E_{1g} and E^1_{2g} peaks appear at 169 and 285 cm^{-1}, respectively [28, 29]. A plan-view high-resolution TEM image of the as-grown multilayer $MoSe_2$ is shown in Fig. 1(e). The inset in Fig. 1(e) is a fast Fourier transform (FFT) pattern taken from the whole image. Figure 1(f) is an inverse FFT from the red dotted square in Fig. 1(e) obtained from the primary reflections only. Figures 1(e) and 1(f) clearly demonstrate that the as-synthesized film has a highly crystalline structure and hexagonal symmetry [30, 31]. This is in good agreement with the bulk characterization results obtained by XRD. In the electron energy loss spectra shown in Figs. 1(g) and 1(h), the Mo $M_{4,5}$ edge at 227 eV (the M_3 and M_2 edges are at 392 and 410 eV, respectively) and the Se L_3 and L_2 edges at 1,436 and 1,476 eV, respectively (the L_1 edge is at 1,654 eV) can be clearly identified, indicating that the as-synthesized film contains Mo and Se. It should be noted that the O K edge at 532 eV, shown in Fig. 1(g), is negligible. This confirms that the MoO_3 precursor is completely

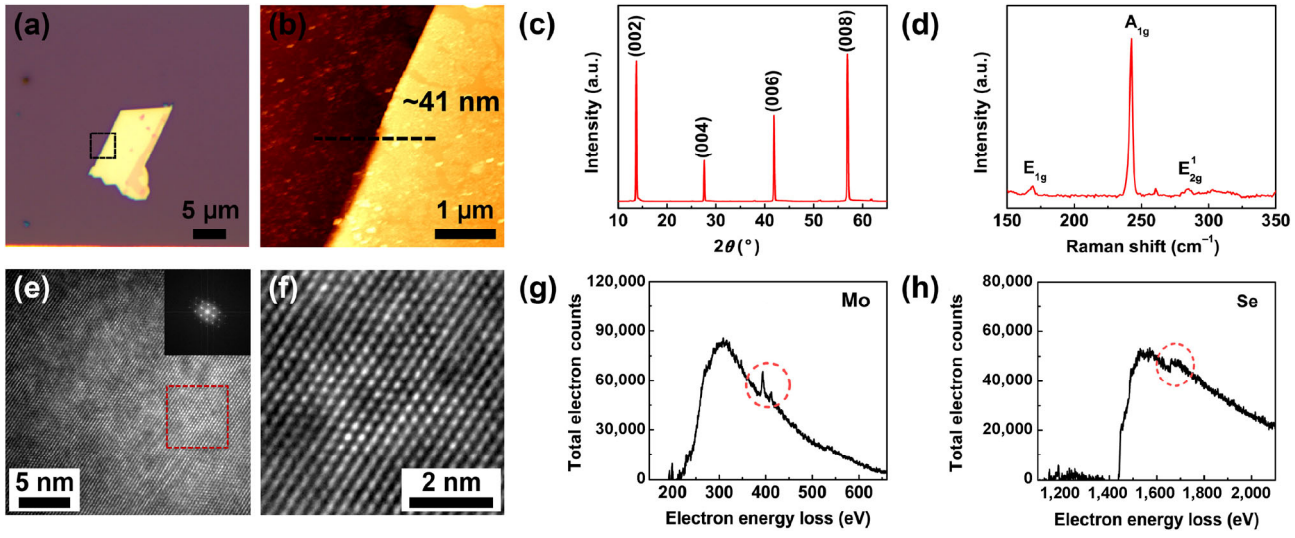

Figure 1 (a) Optical image, (b) AFM image, (c) XRD pattern, and (d) Raman spectrum of a CVD-grown multilayer $MoSe_2$ flake. The image in (b) was taken from the dashed black square in (a), and the thickness of the $MoSe_2$ flake is about 41 nm. (e) Plan-view high-resolution TEM image of the as-synthesized $MoSe_2$ film. Inset in (e) is an FFT from the main panel. (f) Inverse FFT image obtained from the primary reflections in the FFT from the dashed red square in (e). Background-subtracted electron energy loss spectra showing (g) the Mo $M_{4,5}$ edge at 227 eV (Mo M_3 and M_2 edges at 392 and 410 eV loss are shown in the red dotted circle in (g)) and (h) the Se L_3 and L_2 edges at 1,436 and 1,476 eV (Se L_1 edge at 1654 eV loss is shown in the red dotted circle in (h)).

transformed to $MoSe_2$ during the CVD process.

The CVD-grown multilayer $MoSe_2$ samples were used as an active channel in back-gated FETs to detect NO_2 gas. The as-grown bulk $MoSe_2$ was mechanically exfoliated to obtain multilayer $MoSe_2$ flakes, and then Ti/Au (20 nm/300 nm) was deposited onto it to prepare source and drain electrodes. An optical image of the fabricated $MoSe_2$ FET is shown in Fig. S2(a) (in the ESM). The thickness of the $MoSe_2$ flake is about 65 nm, as measured using AFM (Figs. S2(b) and S2(c) in the ESM). For gas-sensing measurements, the electrodes of the device were wire-bonded to gold pads on a leadless chip carrier using gold nanowire, and the device was installed in a gas-sensing chamber. Figure 2(a) shows a three-dimensional (3D) schematic diagram of a $MoSe_2$ transistor-based NO_2 gas sensor. First, we measured the electrical characteristics of the $MoSe_2$ FET. Typical transfer characteristics (I_{ds}–V_{gs}) of the device at V_{ds} = 1.0 V are shown in Fig. 2(b). The device exhibits n-type-dominant ambipolar behavior, indicating that the Ti/Au electrodes form a Schottky barrier such that the barrier height for electrons. Φ_{Bn} is smaller than that for holes (Φ_{Bn}), with an on/off current ratio (I_{on}/I_{off}) > 10^5 and a threshold voltage (V_{th}) of 6.7 V. The output characteristics (I_{ds}–V_{ds}) of the same device are shown in Fig. 2(c). The I_{ds}–V_{ds} curves show linearity at low drain voltages, indicating the formation of an Ohmic contact at room temperature, and exhibit clear saturation behavior at high drain voltages. The field-effect mobility (μ) is estimated to be 65.6 $cm^2 \cdot V^{-1} \cdot s^{-1}$, which is calculated from the triode region using Eq. (1):

$$\mu = \left(\frac{L}{WC_{ox}V_{ds}}\right)\left(\frac{\partial I_{ds}}{\partial V_{gs}}\right) \quad (1)$$

where L is the device channel length (24 μm), W is the device channel width (8 μm), and C_{ox} is the gate capacitance per unit area (1.15×10^{-8} $F \cdot cm^{-2}$).

It was expected that a $MoSe_2$ transistor-based gas sensor would exhibit an ultra-high sensing capacity due to the large surface-to-volume ratio of 2D materials. Figure 3(a) shows the transfer characteristics (I_{ds}–V_{gs}) at V_{ds} = 1 V under different NO_2 gas concentrations. The curve measured in an N_2 environment in the absence of NO_2 exhibits similar characteristics to that in air (Fig. 2(b)). When the device is exposed to NO_2 gas, the off-current in the p-branch (i.e., the hole current) increases significantly with NO_2 gas concen-tration,

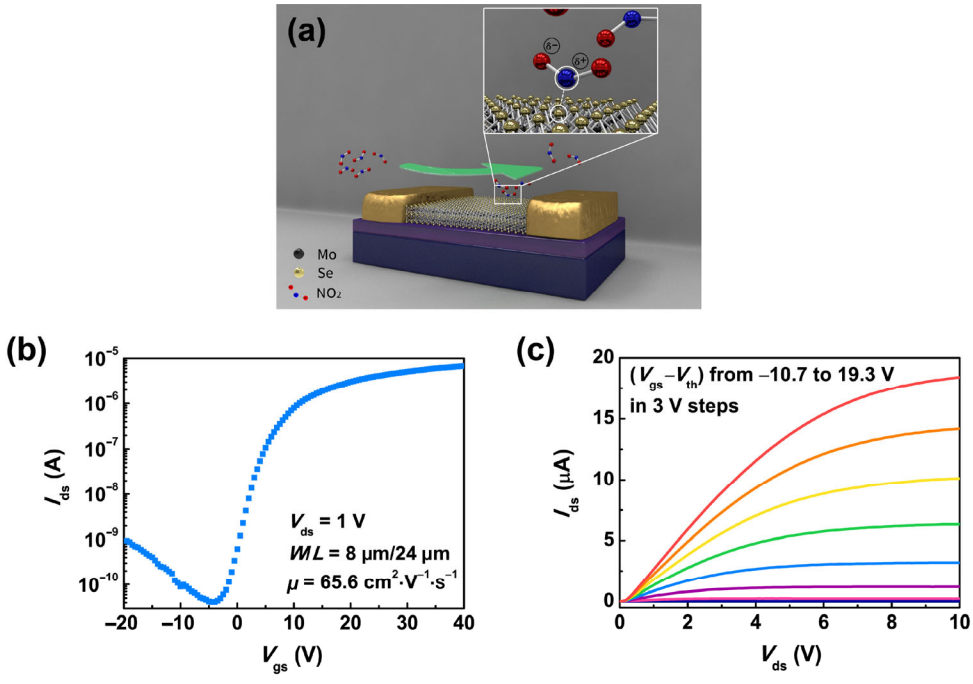

Figure 2 (a) 3D schematic of a $MoSe_2$ FET-based NO_2 gas sensor. (b) Transfer characteristic (I_{ds}–V_{gs}) of a multilayer $MoSe_2$ transistor at V_{ds} = 1 V in a logarithmic scale. (c) Output characteristics (I_{ds}–V_{ds}) at different (V_{gs}–V_{th}) from −10.7 to 19.3 V in 3 V steps.

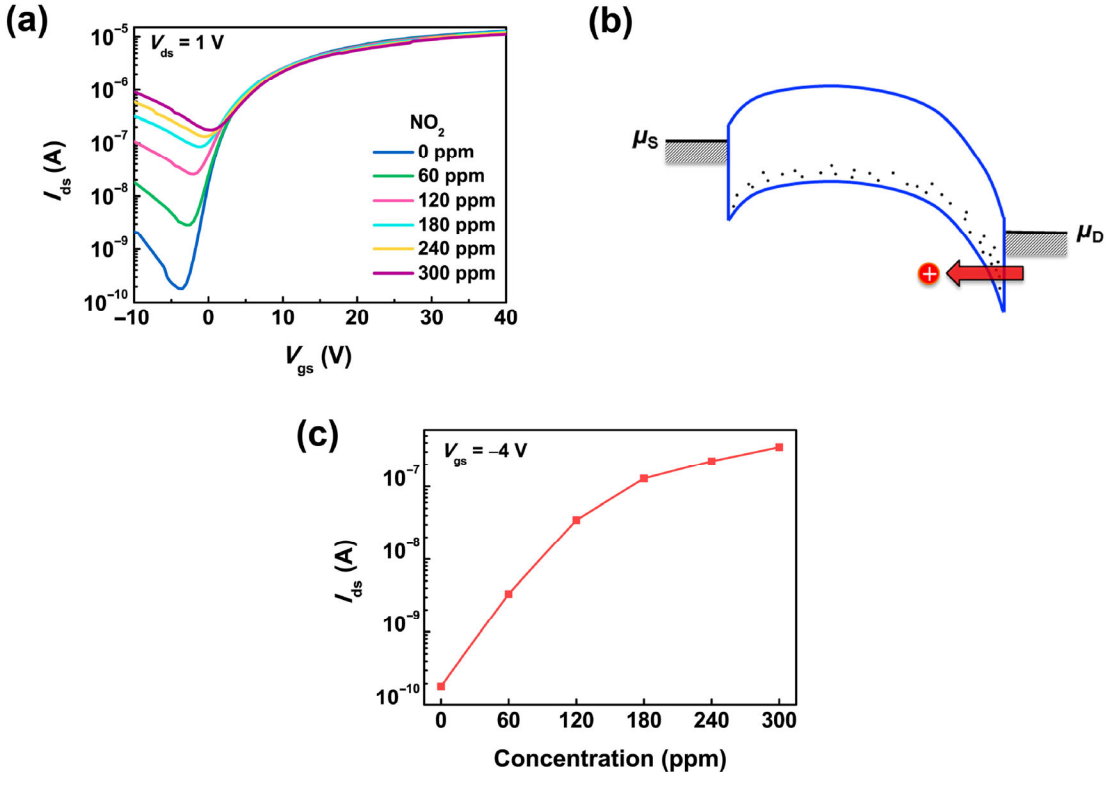

Figure 3 (a) Transfer characteristics (I_{ds}–V_{gs}) measured at NO_2 concentrations of 0, 60, 120, 180, 240, and 300 ppm plotted on a logarithmic scale. (b) Energy band diagram of $MoSe_2$ FET under NO_2 gas at $V_{ds} > 0$ and $V_{gs} < 0$. $\mu_{S,D}$ are the chemical potentials in the source and drain. (c) I_{ds} vs. NO_2 concentration at V_{gs} = −4 V, extracted from (a).

whereas the electron current in the n-branch is largely constant (Fig. 3(a)). It has been reported that NO_2 absorbed in TMDs such as $MoSe_2$, MoS_2, and WSe_2 leads to states in the band gap region close to the valence band [32, 33], and the same was expected for our device.

These states induced by NO_2 molecules can provide extra tunneling paths for hole conduction, as depicted in Fig. 3(b), leading to the hole current increasing as the device is exposed to NO_2 gas. This transport mechanism can also be understood and modeled with the suppression of the effective SB for holes with NO_2, which will be discussed in detail later. Figure 3(c) plots the I_{ds} as a function of NO_2 gas concentration at $V_{gs} = -4$ V. As the NO_2 concentration increases from 0 to 300 ppm, the current is enhanced by a factor of 1,909. This is the maximum current enhancement observed in the off-state regime, and demonstrates the superior sensing capacity of our $MoSe_2$ FETs.

In order to verify the use of FET-based $MoSe_2$ sensors for ultra-high sensitivity gas detection, we have also measured the I_{ds}–V_{ds} characteristics of a diode-like device without applying V_{gs} for different NO_2 gas concentrations, as shown in Fig. 4(a). As the concentration of NO_2 gas increases, the current (I_{ds}) increases in the positive voltage regions but decreases in the negative voltage regions. When a positive voltage is applied on the drain side ($V_{ds} > 0$), the band diagram of the device is analogous to that shown in Fig. 3(b), where hole current increases significantly with NO_2 gas owing to the additional band gap states located near to the valence band, as explained above. Conversely, if the opposite voltage is applied across the device ($V_{ds} < 0$), the chemical potential in the drain becomes higher than that in the source, as shown in Fig. 4(b), where the majority of current is due to electron flow from the drain to the source. In the presence of NO_2 gas, which can enhance charge transfer as a p-dopant, the conduction and the valence band of $MoSe_2$ are shifted upward, causing a wider SB and, thereby, reducing the electron current significantly [8, 12, 32]. Although the same trend can be observed for the on-current (i.e., the electron current in the n-branch) in Fig. 3(a), the impact of charge transfer or doping is minimal when a positive

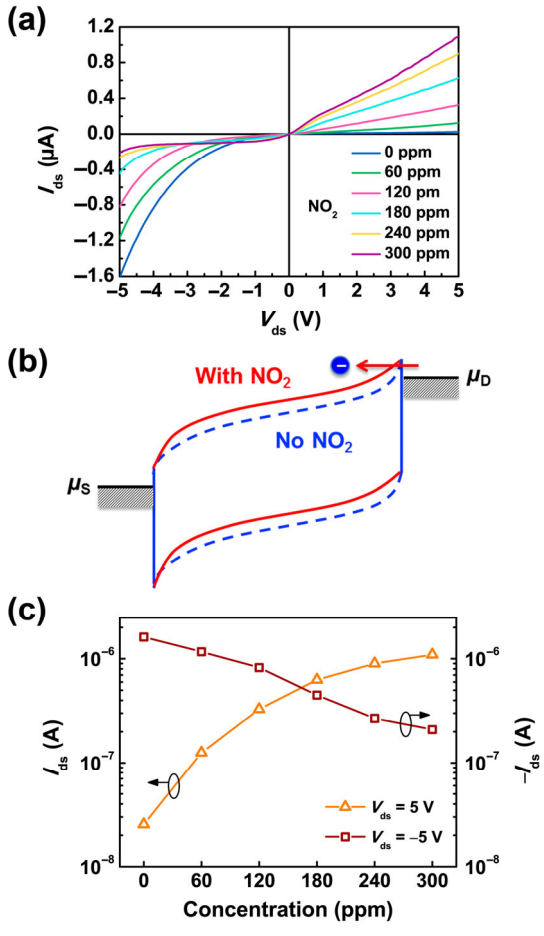

Figure 4 (a) I_{ds}–V_{ds} for NO_2 concentrations from 0 to 300 ppm for a diode-like device with no V_{gs} applied. (b) Band diagram of the diode-like $MoSe_2$ device at $V_{ds} < 0$. Solid red lines show the effect of p-doping with NO_2 gas. (c) I_{ds} vs. NO_2 concentration at $V_{ds} = -5$ and 5 V.

V_{ds} is applied. Figure 4(c) shows the current as a function of the NO_2 gas concentration, measured at $V_{ds} = -5$ and 5 V for the same device as that in Fig. 4(a). For a change in the NO_2 concentration from 0 to 300 ppm, the electron current decreases by 87% at $V_{ds} = -5$ V and the hole current increases by a factor of 43 at $V_{ds} = 5$ V.

Notably, these values are significantly lower than those for a change of current in FET-based $MoSe_2$ sensors, where the current is enhanced by a factor of 1,909 for the same variation in NO_2 concentration, as we have shown above. In addition, Figs. 4(a) and 4(c) clearly indicate that the hole current at positive V_{ds} is a more effective indicator for NO_2 gas using $MoSe_2$ sensors.

For a more in-depth understanding of the characteristics of $MoSe_2$ FET-based sensors, we performed quantum transport simulations using the NEGF method. We modeled the absorption of NO_2 gas in $MoSe_2$ FETs considering (i) the suppression of effective SB height for holes (Φ_{Bp}) due to the extra states and the increased tunneling conferred by the absorbed NO_2, and (ii) the effect of p-doping in the channel region. The effective Φ_{Bp} was varied from 0.74 to 0.34 eV to minimize the hole-leakage paths for NO_2 gas, without changing the SB height for electrons (Φ_{Bn} = 0.1 eV). Figure 5(a) shows the simulated I_{ds}–V_{gs} characteristics in the absence of NO_2 gas and under low and high concentrations of NO_2 gas. They exhibit the same trend as that presented by the experimental data (Fig. 3(a)). The ratio of I_{gas} to I_0 as a function of Φ_{Bp} is plotted in Fig. 5(b) (shown in star symbols), where I_{gas} is the current at different NO_2 concentrations and I_0 is the current without NO_2 gas, obtained from the simulations at V_{gs} = −0.3 V, which is the voltage resulting in the minimum leakage current for I_0. I_{gas}/I_0 exhibits a clear exponential increase with decreasing Φ_{Bp}, according to the following relationship

$$\log_{10}\left(\frac{I_{gas}}{I_0}\right) = p_1 \cdot \Phi_{Bp} + p_2 \quad (2)$$

where p_1 and p_2 are −12.8 and 9.47, respectively. Furthermore, we investigated how the effective Φ_{Bp} is affected by NO_2 gas concentration (c_{NO2}) by correlating the theoretical expression (the dashed line in Fig. 5(b)) with the experimental data (the square symbols in Fig. 5(b)), resulting in

$$\Phi_{Bp} = p_3 \cdot c_{NO_2}^3 + p_4 \cdot c_{NO_2}^2 + p_5 \cdot c_{NO_2} + p_6 \quad (3)$$

where p_3, p_4, p_5, and p_6 are -5.22×10^{-9}, 5.46×10^{-6}, -2.00×10^{-3}, and 0.74, respectively. This indicates that the effective Φ_{Bp} varies significantly with NO_2 gas concentration, gradually reaching saturation as c_{NO2} increases. In addition, a direct relationship between $\left(\frac{I_{gas}}{I_0}\right)$ and c_{NO2} can be obtained from Eqs. (2) and (3) as

$$\frac{I_{gas}}{I_0} = 10^{(p_7 \cdot c_{NO_2}^3 + p_8 \cdot c_{NO_2}^2 + p_9 \cdot c_{NO_2})} \quad (4)$$

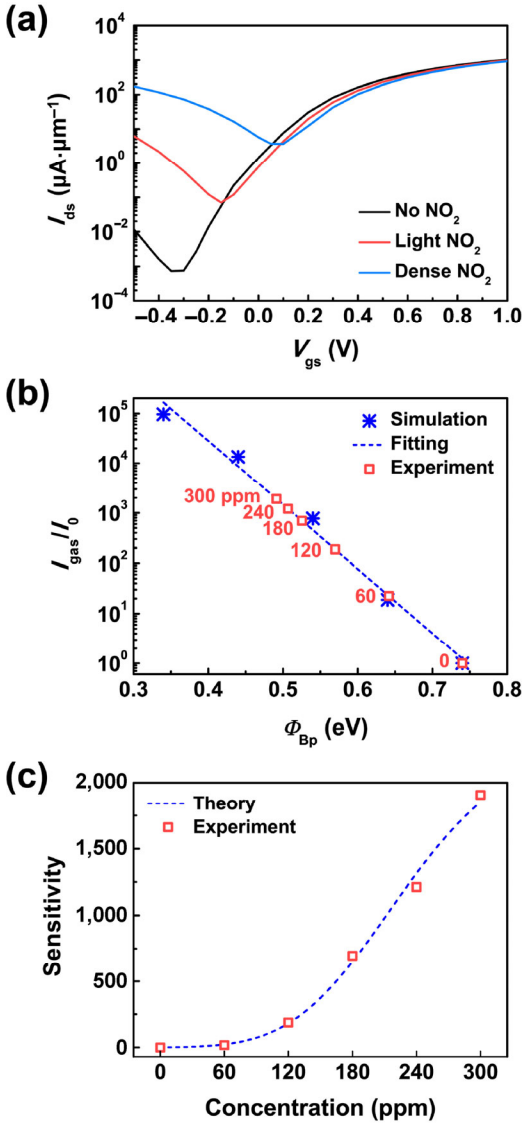

Figure 5 (a) Simulation results of transfer characteristics under zero, low, and high concentrations of NO_2 gas. (b) I_{gas}/I_0 vs. effective SB height for holes (Φ_{Bp}). The blue stars represent simulation results with various Φ_{Bp} obtained at V_{gs} = −0.3 V. The dashed blue line is a linear fit to the simulation results. The red squares represent the experimental data with different gas concentrations, taken from Fig. 3(a) at V_{gs} = −4 V. (c) Sensitivity vs. NO_2 concentration. The dashed blue line is based on theory, and the red square symbols represent the data from the experiments shown in Fig. 3(a) (V_{gs} = −4 V).

where p_7, p_8, and p_9 are 6.68×10^{-8}, -6.99×10^{-5}, and 2.56×10^{-2}, respectively.

The sensitivity (S) of gas sensors can be defined as $(I_{gas} - I_0)/I_0$, which is the most important value in the assessment of gas sensors. We have plotted sensitivity as a function of NO_2 gas concentration in Fig. 5(c)

and Fig. S3 in the ESM. The dashed curve in Fig. 5(c) is a theoretical plot drawn using Eq. (4), and the square symbols are from the experimental data (Fig. 3(a); V_{gs} = −4 V), revealing an excellent match between the theory and experimental observations. Figure 5(c) indicates that our FET-based $MoSe_2$ sensor effectively detects NO_2 gas, showing a linear response to concentration at >100 ppm, with the maximum sensitivity of ca. 1,907 observed at 300 ppm.

We systematically analyzed the time-resolved response of our $MoSe_2$ gas sensor. Figure 6(a) shows the real-time current response of a $MoSe_2$ FET to NO_2 gas, where the concentration of NO_2 gas increases with time. To achieve stable conditions, the different concentrations of NO_2 gas were injected into the chamber for 20 min (light blue regions; not scaled) before the current was measured at V_{gs} = −4 V and V_{ds} = 1 V. The current shows similar behavior to those in Fig. 3(a), indicating the robustness of our $MoSe_2$ gas sensor. As shown in Fig. 6(b), we investigated the on–off switching behavior where the measurement was performed at the same bias conditions as in Fig. 6(a) with an injection gas concentration of 300 ppm. A recovery time of 2 h was typically required under inert N_2 purging gas. However, the recovery time was significantly reduced to 30 min by using a large negative gate bias (V_{gs} = −40 V in Fig. 6(b)). In this case, the repulsive electrical field from the gate bias facilitates the desorption of NO_2 from the $MoSe_2$ surface, and this observation is consistent with those detailed in previous reports [12, 34]. It is feasible that additional treatments such as UV exposure, thermal annealing, or pulse-gating could be applied to further shorten the recovery time [12, 35–37].

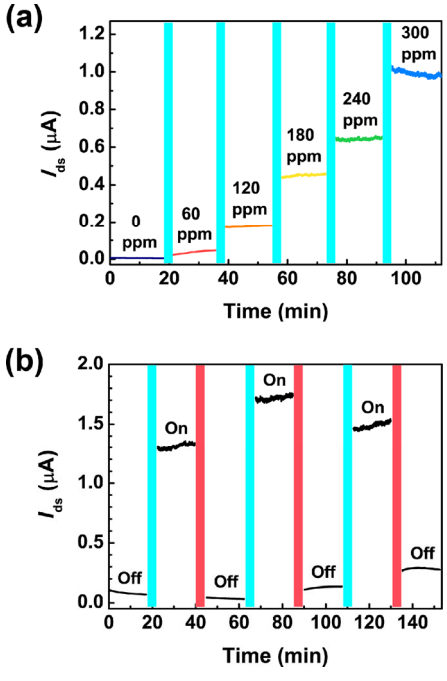

Figure 6 (a) Real-time current response of $MoSe_2$ FET to NO_2 gas at different NO_2 concentrations. The light blue regions indicate 20-min NO_2 gas injection (not scaled) into the chamber before the measurement. (b) Real-time on–off switching behavior conducted at a NO_2 concentration of 300 ppm. The light blue and red regions denote injection for 20 min and venting for 30 min (not scaled), respectively. A large negative gate bias (V_{gs} = −40 V) was applied to desorb NO_2 from the surface of the $MoSe_2$ channel during venting to reduce the recovery time. Current was measured at V_{gs} = −4 V and V_{ds} = 1 V in both (a) and (b).

Finally, selectivity is a very important feature of gas sensors. Generally, selectivity can be improved by two different approaches: firstly, the introduction of functional groups [38] or catalytic particles [39, 40], which can react with the target gas; and secondly, the employment of an appropriate filter that can induce catalytic oxidation (i.e., a catalytic filter) of interfering species [41], or physically remove them (i.e., a porous membrane filter) via molecular key-lock systems [42]. Specifically, for NO_2 gas sensors, many different types of membrane-based filters (e.g., carbonaceous chemical filters, carbon nanocones and discs, or nano-carbonaceous filters) have been reported in the literature [43–45]. Therefore, issues of selectivity toward NO_2 gas can be resolved using previously developed filters designed for NO_2 gas sensors placed upstream of the $MoSe_2$-based FET sensor.

4 Conclusions

We have demonstrated a highly sensitive NO_2 gas sensor based on a CVD-grown $MoSe_2$ FET, which shows n-type-dominant ambipolar behavior with a field-effect mobility of 65.6 $cm^2 \cdot V^{-1} \cdot s^{-1}$ and an on/off current ratio of 10^5. Our experiments showed that the hole current in a $MoSe_2$ FET significantly increases when it is exposed to NO_2 gas, which is attributed to the extra band gap states induced by the absorbed NO_2 gas. We also performed quantum transport

simulations to model the variation of Φ_{Bp} and the effect of p-doping, and the simulations reproduced the experimental observations by considering the induced band gap states. Our study demonstrated the linear response of the sensitivity of the $MoSe_2$ FET to NO_2 gas concentration in the 100–300 ppm range with a maximum sensitivity of ca. 1,907. In addition, a comparison of FET-based sensors and diode-like $MoSe_2$ sensors revealed that sensitivity could be significantly enhanced using a negative V_{gs}, indicating the great advantage of using FET-based chemical sensors. Finally, we have demonstrated excellent real-time response and on–off switching behavior, verifying the robustness of our device. In this study, our highly sensitive $MoSe_2$ FET represents a significant advance in 2D layered materials for practical sensing applications.

Acknowledgements

This research is also supported in part by the National Research Foundation of Korea (Nos. NRF-2013M3C1A3059590, NRF-2014M3A9D7070732, and NRF-2015R1A5A1037548). This work was supported in part by U.S. National Science Foundation under grant CMMI 826276, and in part by NSERC Discovery Grant (No. RGPIN-05920-2014). This research was supported by the Commercializations Promotion Agency for R&D Outcomes (COMPA) funded by the Ministry of Science, ICT and Future Planning (MISP) and in part by the fund from the Korea Institute of Science and Technology (KIST) institutional program. Computing resources were provided by SHARCNET through Compute Canada. D. Y. acknowledges the financial support by WIN Nanofellowship. The authors would like to thank Prof. Jong-Soo Rhyee for supporting CVD $MoSe_2$ flakes.

Electronic Supplementary Material: Supplementary material (schematic of experimental setup, optical and AFM images of $MoSe_2$ device, and sensitivity vs. NO_2 concentration) is available in the online version of this article at http://dx.doi.org/10.1007/s12274-016-1291-7.

References

[1] Cui, Y.; Wei, Q. Q.; Park, H.; Lieber, C. M. Nanowire nanosensors for highly sensitive and selective detection of biological and chemical species. *Science* **2001**, *293*, 1289–1292.

[2] Lavrik, N. V.; Sepaniak, M. J.; Datskos, P. G. Cantilever transducers as a platform for chemical and biological sensors. *Rev. Sci. Instrum.* **2004**, *75*, 2229–2253.

[3] Liu, Y. X.; Dong, X. C.; Chen, P. Biological and chemical sensors based on graphene materials. *Chem. Soc. Rev.* **2012**, *41*, 2283–2307.

[4] Lee, J.; Dak, P.; Lee, Y.; Park, H.; Choi, W.; Alam, M. A.; Kim, S. Two-dimensional layered MoS_2 biosensors enable highly sensitive detection of biomolecules. *Sci. Rep.* **2014**, *4*, 7352.

[5] Kong, J.; Franklin, N. R.; Zhou, C. W.; Chapline, M. G.; Peng, S.; Cho, K.; Dai, H. J. Nanotube molecular wires as chemical sensors. *Science* **2000**, *287*, 622–625.

[6] Tamvakos, A.; Korir, K.; Tamvakos, D.; Calestani, D.; Cicero, G.; Pullini, D. NO_2 gas sensing mechanism of ZnO thin-film transducers: Physical experiment and theoretical correlation study. *ACS Sens.* **2016**, *1*, 406–412.

[7] Collins, P. G.; Bradley, K.; Ishigami, M.; Zettl, A. Extreme oxygen sensitivity of electronic properties of carbon nanotubes. *Science* **2000**, *287*, 1801–1804.

[8] Liu, B.; Chen, L.; Liu, G.; Abbas, A. N.; Fathi, M.; Zhou, C. W. High-performance chemical sensing using Schottky-contacted chemical vapor deposition grown monolayer MoS_2 transistors. *ACS Nano* **2014**, *8*, 5304–5314.

[9] Lu, G. H.; Park, S.; Yu, K. H.; Ruoff, R. S.; Ocola, L. E.; Rosenmann, D.; Chen, J. H. Toward practical gas sensing with highly reduced graphene oxide: A new signal processing method to circumvent run-to-run and device-to-device variations. *ACS Nano* **2011**, *5*, 1154–1164.

[10] Zhang, J.; Boyd, A.; Tselev, A.; Paranjape, M.; Barbara, P. Mechanism of NO_2 detection in carbon nanotube field effect transistor chemical sensors. *Appl. Phys. Lett.* **2006**, *88*, 123112.

[11] Cho, B.; Hahm, M. G.; Choi, M.; Yoon, J.; Kim, A. R.; Lee, Y.-J.; Park, S.-G.; Kwon, J.-D.; Kim, C. S.; Song, M. et al. Charge-transfer-based gas sensing using atomic-layer MoS_2. *Sci. Rep.* **2015**, *5*, 8052.

[12] Late, D. J.; Huang, Y.-K.; Liu, B.; Acharya, J.; Shirodkar, S. N.; Luo, J. J.; Yan, A. M.; Charles, D.; Waghmare, U. V.; Dravid, V. P. et al. Sensing behavior of atomically thin-layered MoS_2 transistors. *ACS Nano* **2013**, *7*, 4879–4891.

[13] Li, H.; Yin, Z. Y.; He, Q. Y.; Li, H.; Huang, X.; Lu, G.; Fam, D. W. H.; Tok, A. I. Y.; Zhang, Q.; Zhang, H. Fabrication of single- and multilayer MoS_2 film-based field-effect transistors for sensing NO at room temperature. *Small* **2012**, *8*, 63–67.

[14] Boarino, L.; Baratto, C.; Geobaldo, F.; Amato, G.; Comini, E.; Rossi, A. M.; Faglia, G.; Lérondel, G.; Sberveglieri, G. NO_2 monitoring at room temperature by a porous silicon gas sensor. *Mater. Sci. Eng. B* **2000**, *69–70*, 210–214.

[15] Comini, E.; Faglia, G.; Sberveglieri, G.; Pan, Z. W.; Wang, Z. L. Stable and highly sensitive gas sensors based on semiconducting oxide nanobelts. *Appl. Phys. Lett.* **2002**, *81*, 1869–1871.

[16] Das, A.; Dost, R.; Richardson, T.; Grell, M.; Morrison, J. J.; Turner, M. L. A nitrogen dioxide sensor based on an organic transistor constructed from smorphous semiconducting polymers. *Adv. Mater.* **2007**, *19*, 4018–4023.

[17] McAlpine, M. C.; Ahmad, H.; Wang, D. W.; Heath, J. R. Highly ordered nanowire arrays on plastic substrates for ultrasensitive flexible chemical sensors. *Nat. Mater.* **2007**, *6*, 379–384.

[18] Zhang, D. H.; Liu, Z. Q.; Li, C.; Tang, T.; Liu, X. L.; Han, S.; Lei, B.; Zhou, C. W. Detection of NO_2 down to ppb levels using individual and multiple In_2O_3 nanowire devices. *Nano Lett.* **2004**, *4*, 1919–1924.

[19] Cho, B.; Yoon, J.; Lim, S. K.; Kim, A. R.; Kim, D.-H.; Park, S.-G.; Kwon, J.-D.; Lee, Y.-J.; Lee, K.-H.; Lee, B. H. et al. Chemical sensing of 2D graphene/MoS_2 heterostructure device. *ACS Appl. Mater. Interfaces* **2015**, *7*, 16775–16780.

[20] Late, D. J.; Doneux, T.; Bougouma, M. Single-layer $MoSe_2$ based NH_3 gas sensor. *Appl. Phys. Lett.* **2014**, *105*, 233103.

[21] Samnakay, R.; Jiang, C.; Rumyantsev, S. L.; Shur, M. S.; Balandin, A. A. Selective chemical vapor sensing with few-layer MoS_2 thin-film transistors: Comparison with graphene devices. *Appl. Phys. Lett.* **2015**, *106*, 023115.

[22] Rhyee, J.-S.; Kwon, J.; Dak, P.; Kim, J. H.; Kim, S. M.; Park, J.; Hong, Y. K.; Song, W. G.; Omkaram, I.; Alam, M. A. et al. High-mobility transistors based on large-area and highly crystalline CVD-grown $MoSe_2$ films on insulating substrates. *Adv. Mater.* **2016**, *28*, 2316–2321.

[23] Datta, S. *Quantum Transport: Atom to Transistor*, 2nd ed.; Cambridge University Press: Cambridge, 2005.

[24] Yun, W. S.; Han, S. W.; Hong, S. C.; Kim, I. G.; Lee, J. D. Thickness and strain effects on electronic structures of transition metal dichalcogenides: 2H-MX_2 semiconductors (M = Mo, W; X = S, Se, Te). *Phys. Rev. B* **2012**, *85*, 033305.

[25] Kumar, A.; Ahluwalia, P. K. Tunable dielectric response of transition metals dichalcogenides MX_2 (M = Mo, W; X = S, Se, Te): Effect of quantum confinement. *Phys. B-Condens. Matter* **2012**, *407*, 4627–4634.

[26] Tongay, S.; Zhou, J.; Ataca, C.; Lo, K.; Matthews, T. S.; Li, J. B.; Grossman, J. C.; Wu, J. Q. Thermally driven crossover from indirect toward direct bandgap in 2D semiconductors: $MoSe_2$ versus MoS_2. *Nano Lett.* **2012**, *12*, 5576–5580.

[27] Bissessur, R.; Xu, H. Nanomaterials based on molybdenum diselenide. *Mater. Chem. Phys.* **2009**, *117*, 335–337.

[28] Tonndorf, P.; Schmidt, R.; Böttger, P.; Zhang, X.; Börner, J.; Liebig, A.; Albrecht, M.; Kloc, C.; Gordan, O.; Zahn, D. R. T. et al. Photoluminescence emission and raman response of monolayer MoS_2, $MoSe_2$, and WSe_2. *Opt. Express* **2013**, *21*, 4908–4916.

[29] Zhao, Y. Y.; Luo, X.; Li, H.; Zhang, J.; Araujo, P. T.; Gan, C. K.; Wu, J.; Zhang, H.; Quek, S. Y.; Dresselhaus, M. S. et al. Interlayer breathing and shear modes in few-trilayer MoS_2 and WSe_2. *Nano Lett.* **2013**, *13*, 1007–1015.

[30] Jung, C.; Kim, S. M.; Moon, H.; Han, G.; Kwon, J.; Hong, Y. K.; Omkaram, I.; Yoon, Y.; Kim, S.; Park, J. Highly crystalline CVD-grown multilayer $MoSe_2$ thin film transistor for fast photodetector. *Sci. Rep.* **2015**, *5*, 15313.

[31] Xia, J.; Huang, X.; Liu, L.-Z.; Wang, M.; Wang, L.; Huang, B.; Zhu, D.-D.; Li, J.-J.; Gu, C.-Z.; Meng, X.-M. CVD synthesis of large-area, highly crystalline $MoSe_2$ atomic layers on diverse substrates and application to photodetectors. *Nanoscale* **2014**, *6*, 8949–8955.

[32] Yue, Q.; Shao, Z.; Chang, S.; Li, J. Adsorption of gas molecules on monolayer MoS_2 and effect of applied electric field. *Nanoscale Res. Lett.* **2013**, *8*, 425.

[33] Sharma, M.; Jamdagni, P.; Kumar, A.; Ahluwalia, P. Interactions of gas molecules with monolayer $MoSe_2$: A first principle study. In *AIP Conference Proceedings, Dae Solid State Physics Symposium 2015*; AIP Publishing: Uttar Pradesh, India, 2016; pp 140045.

[34] Fan, Z. Y.; Lu, J. G. Gate-refreshable nanowire chemical sensors. *Appl. Phys. Lett.* **2005**, *86*, 123510.

[35] Fan, S.-W.; Srivastava, A. K.; Dravid, V. P. UV-activated room-temperature gas sensing mechanism of polycrystalline ZnO. *Appl. Phys. Lett.* **2009**, *95*, 142106.

[36] Fowler, J. D.; Allen, M. J.; Tung, V. C.; Yang, Y.; Kaner, R. B.; Weiller, B. H. Practical chemical sensors from chemically derived graphene. *ACS Nano* **2009**, *3*, 301–306.

[37] Li, J.; Lu, Y. J.; Ye, Q.; Cinke, M.; Han, J.; Meyyappan, M. Carbon nanotube sensors for gas and organic vapor detection. *Nano Lett.* **2003**, *3*, 929–933.

[38] Some, S.; Xu, Y.; Kim, Y.; Yoon, Y.; Qin, H. Y.; Kulkarni, A.; Kim, T.; Lee, H. Highly sensitive and selective gas sensor using hydrophilic and hydrophobic graphenes. *Sci. Rep.*

2013, *3*, 1868.

[39] Wöllenstein, J.; Böttner, H.; Jaegle, M.; Becker, W. J.; Wagner, E. Material properties and the influence of metallic catalysts at the surface of highly dense SnO_2 films. *Sens. Actuators B: Chem.* **2000**, *70*, 196–202.

[40] Ryzhikov, A.; Labeau, M.; Gaskov, A. Al_2O_3 (M = Pt, Ru) catalytic membranes for selective semiconductor gas sensors. *Sens. Actuators B: Chem.* **2005**, *109*, 91–96.

[41] Fleischer, M.; Meixner, H. Selectivity in high-temperature operated semiconductor gas-sensors. *Sens. Actuators B: Chem.* **1998**, *52*, 179–187.

[42] Matsuguchi, M.; Uno, T. Molecular imprinting strategy for solvent molecules and its application for QCM-based VOC vapor sensing. *Sens. Actuators B: Chem.* **2006**, *113*, 94–99.

[43] Dubois, M.; Brunet, J.; Pauly, A.; Spinelle, L.; Ndiaye, A.; Guérin, K.; Varenne, C.; Lauron, B.; Klyushin, A. Y.; Vinogradov, A. S. A carbonaceous chemical filter for the selective detection of NO_2 in the environment. *Carbon* **2013**, *52*, 17–29.

[44] Pauly, A.; Dubois, M.; Brunet, J.; Spinelle, L.; Ndiaye, A.; Guérin, K.; Varenne, C.; Vinogradov, A. S.; Klyushin, A. Y. An innovative gas sensor system designed from a sensitive organic semiconductor downstream a nanocarbonaceous chemical filter for selective detection of NO_2 in an environmental context. Part II: Interpretations of O_3/ nanocarbons and NO_2/nanocarbons interactions. *Sens. Actuators B: Chem.* **2012**, *173*, 652–658.

[45] Brunet, J.; Pauly, A.; Varenne, C.; Ndiaye, A. L.; Dubois, M. Nanocarbonaceous filters for the achievement of highly sensitive and selective NO_2 monitoring by means of phthalocyanine-based resistive sensors. *Procedia Eng.* **2012**, *47*, 29–32.